2019 IEEE/RSJ International Conference on Intelligent Robots and Systems (IROS)
Macau, China, November 4-8, 2019

Characterizing Environmental Interactions for Soft Growing Robots

David A. Haggerty[1,2], Nicholas D. Naclerio[1], and Elliot W. Hawkes[1]

Abstract— **Soft, tip-extending devices, or "vine robots," are a promising new paradigm for navigating cluttered and confined environments. Because they lengthen from their tips, there is little relative movement of the body with the environment, and the compressible nature of the device allows it to pass through orifices smaller than its diameter. However, the interaction between these devices and the environment is not well characterized. Here we present a comprehensive mathematical model that describes vine robot behavior during environmental interaction that provides a basis from which informed designs can be generated in future works. The model incorporates transverse and axial buckling modes that result from growing into obstacles with varying surface normals, as well as internal path-dependent and independent resistances to growth. Accordingly, the model is able to predict the pressure required to grow through a given environment due to the interaction forces it experiences. We experimentally validate both the individual components and the full model. Finally, we present three design insights from the model and demonstrate how they each improve performance in confined space navigation. Our work helps advance the understanding of tip-extending, vine robots through quantifying their interactions with the environment, opening the door for new designs and impactful applications in the realms of healthcare, research, search and rescue, and space exploration.**

I. Introduction

In contrast to traditional rigid robots, which are well suited for strength, precision, and repeatability, soft robots easily adapt to changing environments without complex mechanisms and control schemes [1,2]. Tip-extending, vine-inspired robots, or "vine robots," are a particularly exciting new class of soft robots that can lengthen like a vine to navigate challenging environments. Various skin-eversion robots have been presented [3]–[7], with the most recent showing the ability to lengthen by thousands of percent, steer autonomously, and move at rates comparable to animal locomotion [8]. These pneumatic robots are composed of a thin-walled membrane, inverted inside itself, such that when pressurized, new material passes out through the tip, allowing it to "grow." This characteristic behavior eliminates the need for friction between the robot body and its environment in order to progress along its path. Further, because the tube remains largely stationary with respect to its surroundings, there is little sliding with respect to the environment, and the robot can squeeze through tight spaces. Finally, it is able to passively buckle around difficult obstacles with minimal force applied to the environment, avoiding the control complexity of other continuum robots while ensuring the safety of both the device and its surroundings [9]–[11]. These advantages have led to further work on vine robots including active steering [12], medical applications [13], archaeology [14], and burrowing [15].

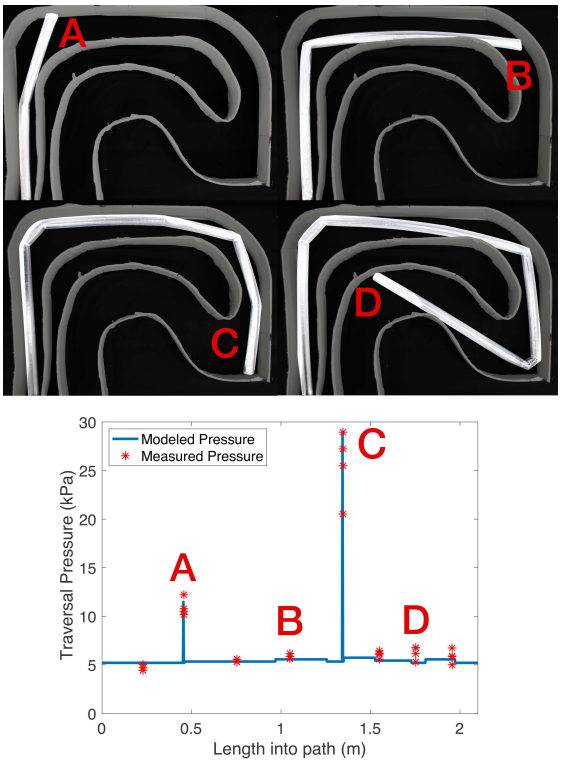

Fig. 1. Characterization of the environmental interactions of a soft tip-extending robot. *Top:* Sequence of photos showing the extending "vine" robot navigating a constrained, tortuous path. *Bottom:* The required pressure to cause growth as a function of position along path. Letters correspond to positions shown in images.

While these demonstrations show the potential of vine robots, a systematic and rigorous formalization of the principles underlying vine robot behavior is lacking. Toward this goal, the contributions of this paper are: i) a refinement of the model for vine robots moving in free space as initially presented by Blumenschein et al. [16], ii) a new model of vine robots moving in constrained spaces that characterizes environmental interaction forces on the robot, and iii) implementations of design insights derived from this model that show substantially improved performance over previous vine robot designs.

What follows is a description of the analytical model we developed, followed by a results section that validates

*This work was supported in part by the National Science Foundation grant no. 1637446.

[1]Authors are with the Department of Mechanical Engineering, University of California, Santa Barbara, Santa Barbara, CA, 93106
[2]Corresponding author, davidhaggerty@ucsb.edu

the model. We then present three design implications in real systems inspired by our analysis. We conclude with a discussion of the strengths and limitations of the current investigation, as well as the planned next steps.

II. Modeling

The goal of this section is to present our mathematical models describing the individual components governing the behavior of vine robots as they move through unconstrained and constrained environments. The modeling will provide the required pressure to extend based off the varying interaction forces produced by contact with its environment, dictated by the morphology and materials of the robot body and the shape of the path through which it is passing. We begin with a description of the device moving through an unconstrained environment, where we refine the model previously presented by Blumenschein et al. [16]. We then build upon this to develop a new model that considers the constrained case where sharp turns and obstacles are present.

A. Extension in an Unconstrained Environment

The physics governing the growth of pressure-driven, tip-everting devices in unconstrained environments can be described by two basic components: a path dependent term and a path independent term. This mathematical description was introduced in Blumenschein et al. [16], inspired by the Lockart-Ortega equation describing plant cell growth. The contribution of this section is to better characterize the effect of large amounts of total curvature on required growth pressure.

The basic equations from Blumenschein et al. [16] can be expressed as follows:

$$\begin{aligned} (PA)_{evert} &= (PA)_{ind} + (PA)_{dep} \\ \text{where}: \quad (PA)_{ind} &= YA + (\frac{1}{\phi}v)^{\frac{1}{n}}A, \\ (PA)_{dep} &= \mu_s wL + \sum_i Ce^{\frac{\mu_c L_i}{R_i}}, \end{aligned} \tag{1}$$

where the subscripts *evert*, *ind*, and *dep* indicate eversion pressure (i.e. pressure required to grow from the tip), the path-independent terms, and the path-dependent terms, respectively. P is the internal pressure, Y is the yield pressure required to evert body material, A is the device's cross-sectional area, ϕ is the material extensibility, v is the tip velocity, n is a power term close to unity, μ_s is the length dependent friction coefficient, w is the normal force exerted per unit length by the internal robot tail (i.e. the length of robot body inverted inside itself), L is the length of the soft robot body, C is a curve-fit constant, μ_c is the curvature dependent friction coefficient, L_i is the length of robot tail experiencing the ith instance of curvature, and R_i is the radius of said curvature.

For this work, we are interested in paths less than 5 m long and average growth speeds less than 0.05 m/s. Accordingly, certain terms dominate in both the path independent and path dependent equations in (1), rendering others negligible. In the path dependent case, the curvature component exponentially increases, overpowering the linear length dependent friction force, allowing us to neglect it. Further, with a growth velocity under 0.05 m/s, the velocity term constitutes roughly 5% of the yield term in the path independent equation, allowing us to also neglect it. As such, the general solution in (1) simplifies to:

$$(PA)_{evert} = YA + \sum_i Ce^{\frac{\mu_c L_i}{R_i}}. \tag{2}$$

To add to this work, we characterize the C coefficient in the path dependent term. Blumenschein et al. used an experimental setup that required a multi-parameter best fit that found values for both C and μ simultaneously. Unfortunately, this resulted in nonphysically large variations in μ and accordingly inaccurate values of C. To address this challenge, we note that the curvature dependence term is based on the capstan equation,

$$T_{out} = T_{hold}\, e^{\mu\theta}, \tag{3}$$

where T_{out} is the output tension after a curve, T_{hold} is the input tension before the curve, and θ is the angle of the curvature experienced. The C coefficient corresponds to T_{hold}, but is not readily measurable in the case of normal extension of the robot, given its very small magnitude. This tension is due to the frictional force of the tail inside the body of the device before the curve. In order to estimate this capstan coefficient, we systematically vary this input tension with known loads and yield values, determine the exponential parameter, then solve for the capstan coefficient when no load is applied. Section III-A describes our experimental setup for this characterization.

B. Extension in a Constrained Environment

Fundamental to the operation of vine robots is movement through constrained environments where movement is impeded by obstacles. Due to the axial stiffness of the materials generally comprising vine robots, body buckling becomes the only appreciable form of reconfiguration around obstacles or in paths with turns. Self-buckling, or buckling caused by the forces the growing robot applies to the environment, occurs in two modes: axial and transverse. The pressure required to cause these self-buckling modes can be much higher than during growth in unconstrained environments, meaning we must consider an additional, higher pressure when the device is required to pass through a tight curve or around an obstacle. We present an appropriate model here.

The simplest buckling mode is that of the transverse case, where buckling occurs due to loading perpendicular to the direction of growth. These deflections have been shown to be predictable [12], however in a kinematic model the internal pressure of the robot and the forces applied to the environment were not considered. Hammond et al. [17], among others [18,19], have shown that this restorative internal moment is simply

$$M_{int} = \pi P R^3 = F_{tr} L, \tag{4}$$

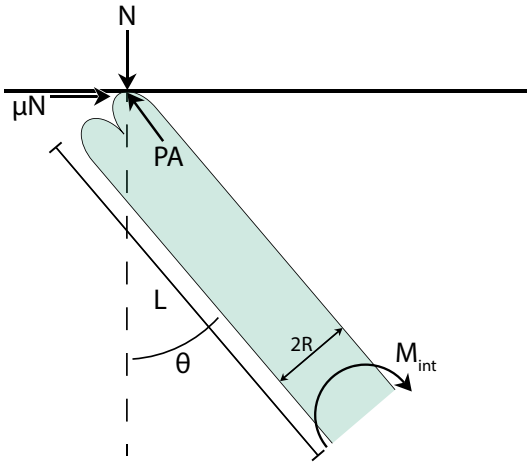

Fig. 2. Illustration of free body diagram used to determine relationship in (6).

where M_{int} is the restorative moment due to internal pressure, r is the device radius, P is the internal pressure, F_{tr} is the transverse load applied, and L is the unconstrained length. In the case of a vine robot navigating a closed path, the force F_{tr} is produced by internal pressure and its magnitude is a function of the angle of incidence with its path boundary. Taking a moment balance about the nearest constrained point along the body of the robot, illustrated by Figure 2, and assuming quasi-equilibrium just prior to the point of buckling yields:

$$M_{int} = NLsin\theta - \mu NLcos\theta, \tag{5}$$

where N is the normal force generated by an interaction with the path and L is the unsupported length. Realizing N is a function of internal pressure, (5) reduces to a simple geometric relationship:

$$\frac{R}{L} = \frac{sin\theta - \mu cos\theta}{cos\theta + \mu sin\theta}, \tag{6}$$

where θ is taken to be the angle of incidence with respect to the surface normal and μ is the coefficient of friction between the device and its boundary.

However, this relation simply represents the smallest value of the ratio of radius to unsupported length at a given angle, and as such can be treated as a lower angle bound. This allows for a conditional requirement to be developed: for a given robot radius and unsupported length, transverse buckling will occur at any angle of incidence larger than that which satisfies the equality in (6), denoted θ_{min}.

The other mode of buckling encountered in constrained paths is axial buckling. Axial buckling mechanics for soft, inflated bodies differ markedly from those of traditional, rigid beams. While rigid body axial buckling is easily expressed through the Euler equation, the compressibility of air and the large ratio of tensile to compressive strength of polymer films is not captured in this model.

Here we invoke the work of Fichter [20], who presents a Euler-inspired, linearized axial buckling model for inflatable beams derived from a virtual work approach. This theory characterizes the inflatable beam critical load F_{cr} (i.e., the load that causes a complete loss of tension in one side of the beam and thus wrinkling) as the ratio product of beam stiffnesses (Euler buckling stiffness and shear stiffness, $P + G\pi rt$) to the sum of beam stiffnesses in a purely axial loading condition, expressed as:

$$F_{cr} = \frac{EI\frac{\pi^2}{L^2}(P + G\pi Rt)}{EI\frac{\pi^2}{L^2} + P + G\pi Rt}, \tag{7}$$

where, E is Young's Modulus, I is the second moment of area of the inflatable beam, L is the unconstrained length of the member, P is the force due to internal pressure, G is the shear modulus, r is the radius of the cylinder, and t is the wall thickness. When the everting robot extends into an obstacle, there is not an external load applied to the beam, but rather there is an interaction force produced by the robot attempting to lengthen. Thus the critical load becomes the force produced by internal pressure:

$$P_{cr}A = \frac{EI\frac{\pi^2}{L^2}(P_{cr}A + G\pi Rt)}{EI\frac{\pi^2}{L^2} + P_{cr}A + G\pi Rt} \quad where \quad F_{cr} = P_{cr}A \tag{8}$$

Solving this equation for critical buckling pressure, P_{cr}, generates a second degree polynomial. Isolating P_{cr} via the quadratic equation and taking the right-half plane solutions yields

$$P_{cr} = \frac{1}{2}\left[\sqrt{\left(\frac{G\pi Rt}{A}\right)^2 + \frac{4EGI\pi^3 Rt}{A^2L^2}}\right] - \frac{G\pi Rt}{2A}. \tag{9}$$

From this equation, we immediately see that resistance to buckling decreases with larger unsupported free lengths and lower elastic and shear moduli. As well, while not as readily apparent, upon plotting P_{cr} with varying R, we see smaller device diameters similarly lower resistance to buckling. Experimental validation of this relationship is presented in Section III-B.

C. Full Model for Tortuous Path with Self-buckling

With the models from Sections II-A and II-B, we are prepared to write a single equation for the case of a tortuous path with turns that produce both axial and transverse self-buckling. To form this full model, we estimate the direction of the contact normal between the tip of the device and the path. At larger contact angles, transverse buckling occurs and the device will follow the obstacle with it's tip [12]. When the angle between the surface normal and the direction of growth, S, falls below θ_{min} (see (6)) axial self-buckling occurs instead. When axial buckling occurs, we add the self-buckling pressure from (9) to the predicted pressure on a smooth path from (2):

$$P_{evert} = \frac{F_y}{A_{cs}} + \sum_i C e^{\frac{\mu L_i}{R_i}} + \begin{cases} P_{cr,i} \text{ for } S < \theta_{min}, \\ 0 \text{ otherwise.} \end{cases} \quad (10)$$

Here the effect of curvature is applied based on the summation of curvatures experienced by the remaining inverted tail, and buckling pressure only influences growth pressure at the leading instance of curvature producing a surface normal contact angle less than θ_{min}.

Tracking the remaining inverted tail is completed by creating a piecewise relationship between total device length and starting device length, knowing for each increment in robot body length there is a corresponding increment or decrement in tail length (for example, as the robot grows the tail length will first increase, matching the length of grown robot until half the material is deployed, and then will decrease until no tail remains inside the robot). While this composite model is only an approximation, future sections will show it usefully captures the observed basic behavior of the device (see Section III-C).

III. Results

This section presents experiments verifying both the individual elements of the model ((10)) as well as the model as a whole, which predicts growth pressure as a function of device materials and morphology, and the shape of the path traversed.

A. Characterization of Capstan Coefficient

To characterize the capstan coefficient and expand upon the model presented by Blumenschein et al. in (2), we first determined the yield pressure inherent in our robot. Blumenschein et al. showed that yield force (force required to evert material from the tip), while dynamically complex, is a constant dependent on material, with yield pressure a function of cross sectional area. As such, multiple devices were tested with varying tail lengths, with pressure slowly increased until the device sustained tip growth.

These values were recorded using a Dwyer Instruments 626 Series pressure transmitter (0-205 kPa range, 0.25% full scale accuracy), and the minimum, maximum, and mean values were found to be 2.301, 4.036, and 3.210 kPa, respectively, based on 27 trials with a standard deviation of 0.509. These tests were conducted in both horizontal and vertical orientations with little variation, likely due to tail weight contributing negligibly to the relatively high-force required to unfurl the tip material; rather, the range of values measured appeared to be mainly dependent on material condition at the tip. Thus, both vertical and horizontal orientation test values were used in averaging the yield pressure.

Next, we tested the pressure required to grow with various resisting tensions applied to the tail of the device. Two values of T_{hold} which were expected to dominate the latent tension produced by the loose tail were chosen. These values were produced by two masses (15 g and 20 g) suspended from the tail. A 9.25 cm rigid cylinder was cantilevered from a table with its axis parallel to the ground. The masses (first 15 g then 20 g) were adhered to the fully everted tip of the device, which was then completely inverted. With the axis of the device vertically oriented, such that the mass would produce a pure tension in the tail, wrap angles, in radians, between π and 4π, incremented by π, were tested (see Figure 3 for an illustration of the experimental setup). In each case, the pressure was slowly increased to the point of sustained tip growth, with pressure measurements recorded using the same Dwyer Instruments 626 Series pressure transmitter.

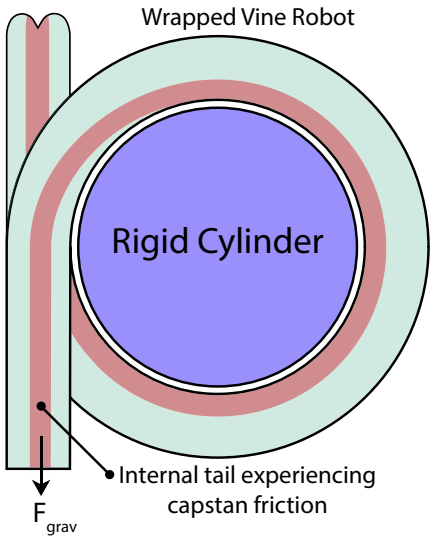

Fig. 3. Illustration of capstan coefficient experimental setup. In this drawing, the suspended mass would be found in the lower left of the sketch noted as F_{grav}.

TABLE I
Wrap Test Results (kPa)

Wrap Angle (rad)	π	2π	3π	4π
20 g mass	5.882	9.145	14.917	20.106
15 g mass	4.615	5.828	8.543	13.101
0 g mass	3.552	4.900	6.387	9.076

Four tests for each mass, at each wrap angle, were conducted, followed by the same regimen for a device with zero added mass. Figure 4 shows these results graphically, alongside the model presented in (10), while Table I presents the average value of each trial.

The exponential parameter, μ_c in (10) was determined in the first two cases by using the known values of T_{hold} and Y via curve fit in Matlab. This produced a value for μ_c of 0.222 in the 15 g case, 0.245 for 20 g, producing a mean value of 0.234 and a 9.25% difference between the two. Using this average value for μ_c and the measured values for Y, the value of T_{hold} was the subsequently determined to be 0.0824 N.

B. Validation of Self-buckling Model

Transverse buckling in vine robots occurs when a transverse interaction force produces a moment about the nearest supported point that exceeds that produced by internal pressure, as expressed in (4). Knowing that this force is similarly produced by internal pressure, no additional pressurization

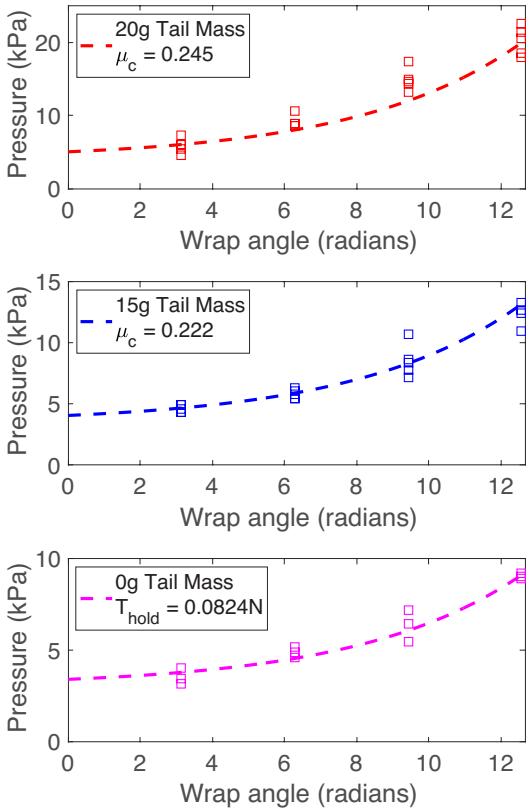

Fig. 4. Three wrap tests, conducted with varying tail weights, with wrap angles ranging from π radians to 4π radians. *Top and middle:* Here, known tail masses give a known T_{hold}, allowing a single parameter fitting to yield values for μ_c. *Bottom:* Using the average value of μ_c found from the two cases above, we perform a single parameter fitting to yield the value of T_{hold} for no tail mass.

is expected to produce a transverse buckle, but instead the geometric relation shown in (6) need be satisfied. To verify this, a robot with a diameter of 2.4 cm was grown into a barrier at four different unsupported lengths across four different angles.

In each case, the robot was secured at the specified buckle lengths (15.24, 22.86, 30.48, and 38.10 cm) oriented to the test angle with respect to the surface normal. Pressure was increased to just above the yield point and the robot was allowed to grow into a barrier. A success was recorded in the event of a natural buckle at no increased pressure, and a failure when no buckle occured. These results are presented in Fig. 5, alongside the theoretical minimum angle as predicted by (6).

The predicted axial buckling pressure in (9) depends on the Young's and shear moduli of the material, the device diameter, and the the length of the buckle section. The literature value of Young's modulus of LDPE used in this model was 303 MPa, alongside a shear modulus of 206 MPa [21,22].

Inserting these measured quantities into (8), and formulating (10) with zero curvature, expected values for critical pressure, P_{cr}, were developed for body lengths ranging from 25 cm to 76 cm and a device diameter of 2.4 cm. The robot body was inverted, constrained at the buckle length in question, pressurized to the point of slow, sustained growth, and allowed to grow into a barrier perpendicular to the direction of growth. Pressure was then slowly increased until the point of buckling, with measurements recorded using the pressure transmitter introduced in Sec. III-A. This test was repeated four times for each length.

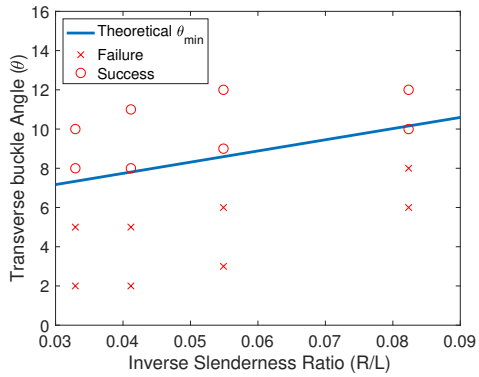

Fig. 5. Experimental results of geometric conditions required to achieve transverse buckling. Unsupported length increases from right to left. The model from (6) is shown as the blue line.

TABLE II
CRITICAL BUCKLING PRESSURE (KPA)

Buckle Length (cm)	25.4	38.1	50.8	63.5	76.2
$P_{cr,ave}$, *measured*	27.689	15.763	9.993	6.170	4.654
P_{cr}, *predicted*	29.418	14.738	9.472	7.011	5.668

The results of these tests are displayed graphically in Figure 6, alongside the modeled behavior curve from (10), and average values are presented in Table II. As seen in Figure 6, at large body lengths the device tracks closely with modeled values, however, at small body lengths the observed quantities begin to show higher variation.

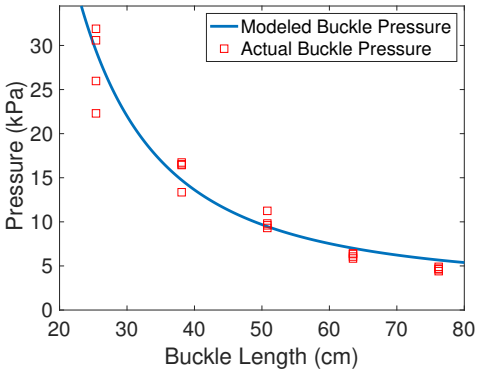

Fig. 6. Experimental results of pressure required for axial buckling versus free length. The model from (10) is shown as a blue line.

C. Validation of Composite Model in a Constrained Path

The outcomes of Sections III-A and III-B were then combined to create a discretized path traversal model. Using (10) as the governing equation for the behavior of our device,

a script was developed in Matlab to predict behavior. The shape of the path was discretized into a series of nominally straight sections interrupted by short curved sections. The instances of curvature were treated as point sources with known wrap angle. To track the amount of tail experiencing curvature, a simple linear relationship was developed relating initial device length to tail length reduction, knowing each unit increase in device length produces a unit decrease in remaining inverted tail (note: the vine robots in this investigation utilized a loose inverted tail, as opposed to the tail reel some vine robots employ [17]). The free length of the device, required for the critical buckling pressure in (10) and the transverse condition in (6), was estimated by the distance between curves. This composite model produced a tip location-specific pressure estimate to traverse the entire path. The value of S from (10) was estimated by estimating the obstacle tangent at the point of contact and measuring the resulting contact angle.

A rigid path was created for evaluation out of foam-core board. An arbitrary path was designed to include both axial and transverse buckling events, as well as to accumulate curvature. Using foam-core board as the substrate, 7.5 cm tall sections of foam-core was then used to form the outline of the path, and a clear acrylic sheet was used to enclose it. After construction, physical measurements for the path were input into the discrete model, and four tests were conducted to validate its accuracy. The device was inserted into one end of the physical model, and pressure was slowly increased until the point of sustained growth. Measurements were taken along straight lengths approximately every 20 cm, and peak pressure was recorded in instances of buckling. Fig. 7 shows the outcomes of each of these trials, overlaid on the predicted values created by the discrete model from (10) across the course presented in Fig. 1.

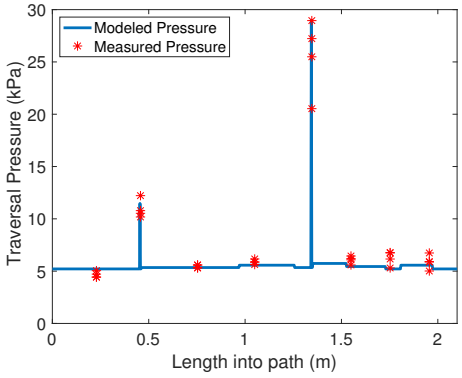

Fig. 7. Experimental validation of the composite model, as also shown in Figure 1. The expected pressure produced by the composite model is shown by the blue line.

IV. Design Implications

The model presented in (10) provides insights on how different design parameters of a vine robot affect its ability to navigate a given path. Below, we examine three such insights, as well as provide comparative tests for each.

A. Increased Membrane Compliance

The effect of membrane compliance on pressure reduction has as of yet not been investigated. To date, vine robots have been designed using a membrane material for which the modulus was selected to be high enough that negligible axial extension would occur while in operation. Such stiffness similarly meant that negligible bending occurred before buckling. While these materials are useful for creating free-standing structures [8], we see from the results of Sec. II, that decreasing this modulus can have advantages when navigating a tortuous path. Examining (9), we see that the modulus of elasticity of the membrane increases the required pressure to buckle. Further, a lower modulus allows additional bending to occur in the body before buckling.

Such bending changes the tip contact angle, and can enable transverse buckling to occur in a situation that initially would have resulted in axial buckling. Critically, as can be seen in (6), transverse buckling requires no additional pressure to initiate, provided its geometric condition is met. We thus constructed two robot bodies out of anisotropic ripstop nylon - one with increased compliance, one traditionally rigid - and compared their ability to navigate the same tortuous path.

Each robot was constructed out of 50 μm thick, silicone impregnated ripstop nylon fabric. By varying the thread orientation, compliance can be built in to the robot body. In the rigid case, the grid pattern was arranged parallel to the longitudinal axis, and at 45° to take advantage of the fabric bias [23] in the compliant case; this modification allows for variable strains when subjected to the same forces. As can be seen in Figure 8, the device built from axially elastic fabric performs significantly better than the inelastic, reducing the maximum pressure required to navigate the same path by a factor of nearly 7.

While these results are exciting, they are only preliminary and there is yet work to be done to fully characterize their behavior. Specifically, measuring their mechanical properties and verifying their behavior with the model presented are the immediate next steps, as the effect of a low material modulus may eliminate the axial consideration in (10) due to the significant bending produced prior to axial buckling.

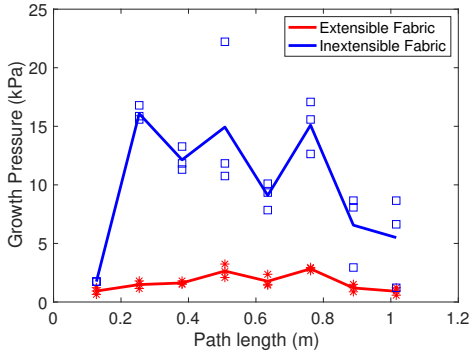

Fig. 8. Effect of membrane compliance for traversing a path consisting of all axial buckling events. The solid lines denote the mean value for each case.

B. Decreased Scale

The effect of scale on a vine robot's ability to navigate a constrained environment has not been previously investigated. Accordingly, we examine (10) and note that the diameter of the robot body has conflicting effects on different terms. A smaller diameter increases the internal pressure required to evert [16], however, a smaller diameter decreases the angle required for a transverse buckle to occur and, while not immediately clear in (9), a small diameter similarly reduces the pressure required to create an axial buckle. From this insight we conclude that, for a given path, the design objective should be to minimize device radius to the furthest extent possible, informed by maximum allowable pressures within the path. To investigate this, three different diameter devices were subjected to the same path and their traversal pressures were recorded, with results found in Figure 9. What was found is a balance exists between growth pressure and buckle pressure, wherein an optimal scale can be found. Specifically, growth pressure goes with r^2 whereas buckle pressure goes with r, and burst pressure goes with $1/r$ (as hoop stress goes with r). The 4.86 cm robot exceeded its burst pressure at the first buckle, while the 1.62 and 2.4 cm robot were both successful, and the 2.4 cm variant traversed at the lowest gauge pressure. It is similarly worth noting the 1.62 and 2.4 cm robot completed the path at roughly the same percentage of burst pressure ($\sim$65%).

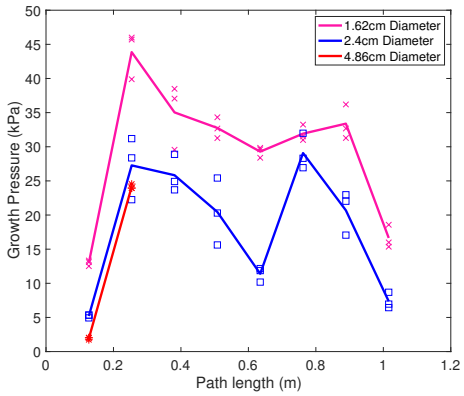

Fig. 9. Effect of diametral scaling for traversing a path consisting of all axial buckling events. Solid lines denote the mean value for each case. Note: the 4.86 cm scale burst at the first buckle.

C. Decreased Internal Tail Length

The most pernicious element of the model provided in (10) for navigating closed, tortuous paths is the pressure required to overcome capstan friction. The exponential nature of the capstan component quickly approaches the burst pressure of these devices, and as such puts a strict limit on the lengths of tortuous paths accessible. Figure 4 verifies this relationship. As such, we investigate the impacts of eliminating this tail friction by rolling the inverted material into a tight wind, allowing it to 'ride' along with the tip of the device as it grows, illustrated in Figure 10. While there are many conceivable methods to store this tail material, such as S-folds, bellows, or simply stuffing the material at the tip, the rolled configuration was chosen for its ease in preparation using mechanical means.

Figure 11 highlights the effect of eliminating the tail for navigating tortuous paths. Two vine robots traversed a path constrained between concentric cylinders. The first robot was tested with a traditionally inverted tail, wherein the robot body is forced through the core of its body. In the second case, the robot body was first tightly rolled up, and the remaining 15 cm were inverted over the rolled material. As the body was inflated, the roll unwound at the tip of the device as it grew.

The traditional vine robot exhibited an exponential increase in growth pressure and burst after three complete revolutions, while the rolled tail robot extended through its full length to six revolutions with near constant pressure. It must be noted, however, that having the rolled tail ride along at the tip affects the dynamics of tip eversion and growth, thereby increasing the pressure required to do so. These results are exciting, and continued exploration can commence in this area.

V. Discussion and Conclusion

Vine robots are an exciting new paradigm in the field of soft robotics, as their unique growth modality opens the door to a wide array of applications. The aim of this work was to better understand their various passive behaviors and lay a foundation upon which future work towards active and autonomous operation and control can be built.

The characterization of the two buckling conditions, as well as the effects of scale, compliance, and capstan friction elimination will allow for more than traversal pressure prediction - it will inform the design as these robots are deployed across the applications introduced in Section I. Further, the fundamental understanding of the forces at play in creating body deflections offers insight into design requirements for creating mechanical components capable of manipulating, articulating, and shape locking these robots, from which unique active/passive hybrid system can be designed.

While our initial results are promising for predicting the macroscopic behavior of these robots in constrained environments, the model presented fails to capture some modes, such as the coupling between buckles in close proximity. Future investigations can be conducted to refine our generalized model to capture these behaviors. Further, to date the working fluid examined has been exclusively air, and the question of using water to drive growth is another open topic for inquiry.

In this work, we presented a mathematical model of the interaction between a soft, tip-extending vine robot and its environment. Our experimental results confirm this model and show that it can predict the effect of environmental contact forces on the behavior of the robot. Importantly, the model can inform the design of robots tailored to specific environments. The model suggests that increasing membrane compliance, containing the tail in the tip, and intelligently choosing the diameter of the robot will allow it to most easily

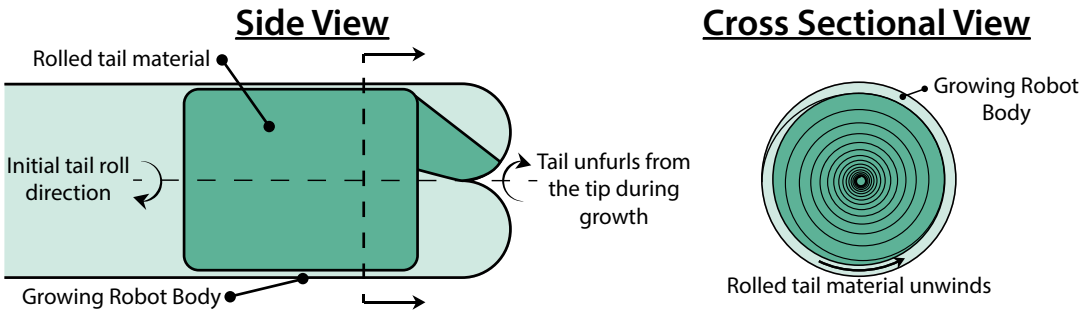

Fig. 10. Illustration of method used to evaluate effect of reducing internal tail length. The Side View shows how the unfurling "pulls" the tail roll along, and the Rear View expresses the rolling method.

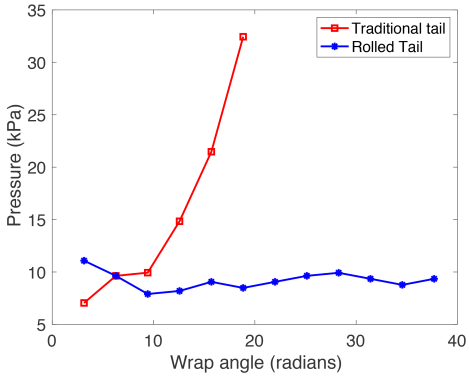

Fig. 11. Wrap test showing effect of reduced internal tail length.

navigate constrained environments. This work contributes to the field by providing a more fundamental and informed starting point for the development of new soft, tip-extending vine robots for navigating difficult environments with varied requirements, ranging from navigating through rubble during search and rescue missions to more delicate applications such as medical endoscopy.

ACKNOWLEDGMENT

Thank you to Laura H. Blumenschein for her helpful advice.

REFERENCES

[1] D. Trivedi, C. D. Rahn, W. M. Kier, and I. D. Walker, "Soft robotics: Biological inspiration, state of the art, and future research," *Applied bionics and biomechanics*, vol. 5, no. 3, pp. 99–117, 2008.

[2] C. Laschi, B. Mazzolai, and M. Cianchetti, "Soft robotics: Technologies and systems pushing the boundaries of robot abilities," *Sci. Robot.*, vol. 1, no. 1, p. eaah3690, 2016.

[3] D. Mishima, T. Aoki, and S. Hirose, "Development of pneumatically controlled expandable arm for search in the environment with tight access," in *Field and Service Robotics*. Springer, 2003, pp. 509–518.

[4] T. Viebach, F. Pauker, G. Buchmann, G. Weiglhofer, and R. Pauker, "Everting sleeve system," Patent, July 5, 2006, european Patent 1676598A2. [Online]. Available: https://patents.google.com/patent/EP1676598A2/en?assignee=invendo&oq=invendo&sort=old

[5] H. Tsukagoshi, N. Arai, I. Kiryu, and A. Kitagawa, "Smooth creeping actuator by tip growth movement aiming for search and rescue operation," in *2011 IEEE International Conference on Robotics and Automation*. IEEE, 2011, pp. 1720–1725.

[6] ——, "Tip growing actuator with the hose-like structure aiming for inspection on narrow terrain," *IJAT*, vol. 5, no. 4, pp. 516–522, 2011.

[7] A. Sadeghi, A. Tonazzini, L. Popova, and B. Mazzolai, "Robotic mechanism for soil penetration inspired by plant root," in *2013 IEEE International Conference on Robotics and Automation*. IEEE, 2013, pp. 3457–3462.

[8] E. W. Hawkes, L. H. Blumenschein, J. D. Greer, and A. M. Okamura, "A soft robot that navigates its environment through growth," *Science Robotics*, vol. 2, no. 8, p. eaan3028, 2017.

[9] M. C. Yip and D. B. Camarillo, "Model-less feedback control of continuum manipulators in constrained environments," *IEEE Transactions on Robotics*, vol. 30, no. 4, pp. 880–889, 2014.

[10] M. Mahvash and P. E. Dupont, "Stiffness control of a continuum manipulator in contact with a soft environment," in *2010 IEEE/RSJ International Conference on Intelligent Robots and Systems*. IEEE, 2010, pp. 863–870.

[11] R. J. Webster III and B. A. Jones, "Design and kinematic modeling of constant curvature continuum robots: A review," *The International Journal of Robotics Research*, vol. 29, no. 13, pp. 1661–1683, 2010.

[12] J. D. Greer, L. H. Blumenschein, A. M. Okamura, and E. W. Hawkes, "Obstacle-aided navigation of a soft growing robot," in *2018 IEEE International Conference on Robotics and Automation (ICRA)*. IEEE, 2018, pp. 1–8.

[13] P. Slade, A. Gruebele, Z. Hammond, M. Raitor, A. M. Okamura, and E. W. Hawkes, "Design of a soft catheter for low-force and constrained surgery," in *2017 IEEE/RSJ International Conference on Intelligent Robots and Systems (IROS)*. IEEE, 2017, pp. 174–180.

[14] M. M. Coad, L. H. Blumenschein, S. Cutler, J. A. R. Zepeda, N. D. Naclerio, H. El-Hussieny, U. Mehmood, J. Ryu, E. W. Hawkes, and A. M. Okamura, "Vine robots: Design, teleoperation, and deployment for navigation and exploration," in preparation.

[15] N. D. Naclerio, C. Hubicki, Y. Aydin, D. Goldman, and E. Hawkes, "Soft robotic burrowing device with tip-extension and granular fluidization," in *2018 IEEE International Conference on Intelligent Robots and Systems (IROS)*, 2018, pp. 5918–5923.

[16] L. H. Blumenschein, A. M. Okamura, and E. W. Hawkes, "Modeling of bioinspired apical extension in a soft robot," in *Conference on Biomimetic and Biohybrid Systems*. Springer, 2017, pp. 522–531.

[17] Z. M. Hammond, N. S. Usevitch, E. W. Hawkes, and S. Follmer, "Pneumatic reel actuator: Design, modeling, and implementation," in *Robotics and Automation (ICRA), 2017 IEEE International Conference on*. IEEE, 2017, pp. 626–633.

[18] R. Comer and S. Levy, "Deflections of an inflated circular-cylindrical cantilever beam," *AIAA journal*, vol. 1, no. 7, pp. 1652–1655, 1963.

[19] R. W. Leonard, G. W. Brooks, and H. G. McComb Jr, "Structural considerations of inflatable reentry vehicles," 1960.

[20] W. Fichter, "A theory for inflated thin-wall cylindrical beams," 1966.

[21] Overview of materials for low density polyethylene LDPE, blow molding grade. MatWeb LLC. [Online]. Available: http://www.matweb.com/search/datasheet_print.aspx?matguid=b34a78d271064c4f85f28a9ffaf94045

[22] N. Ladizesky and I. Ward, "Determination of poisson's ratio and young's modulus of low-density polyethylene," *Journal of Macromolecular Science, Part B: Physics*, vol. 5, no. 4, pp. 661–692, 1971.

[23] J. Page and J. Wang, "Prediction of shear force and an analysis of yarn slippage for a plain-weave carbon fabric in a bias extension state," *Composites Science and Technology*, vol. 60, no. 7, pp. 977–986, 2000.